Atomic collisions with relativistic heavy ions: Target inner-shell ionization

R. Anholt, W. E. Meyerhof, Ch. Stoller, E. Morenzoni,* S. A. Andriamonje,†
J. D. Molitoris, and O. K. Baker
Department of Physics, Stanford University, Stanford, California 94305

D. H. H. Hoffmann
Gesellschaft für Schwerionenforschung, Darmstadt, West Germany

H. Bowman, J.-S. Xu,‡ Z.-Z. Xu,‡ K. Frankel, D. Murphy, K. Crowe, and J. O. Rasmussen
Nuclear Sciences Division, Lawrence Berkeley Laboratories and The University of California, Berkeley, California 94720
(Received 23 May 1984)

Target K-vacancy and L-x-ray production cross sections in collisions with relativistic (82—670-MeV/amu) heavy ions ranging from Ne to U are measured and compared with atomic theories of inner-shell ionization based on the plane-wave Born approximation. Because the counting methods used are unique in atomic physics, careful studies of experimental uncertainties are made. Corrections to the measured cross sections due to x-ray pileup and secondary interactions in the solid targets are also discussed.

I. INTRODUCTION

In the present series of papers, we explore the gross features of x-ray production in relativistic heavy-ion—atom collisions. Projectile and target K-x-ray production have been explored thoroughly at low energies, and interpreted using the molecular model of slow ion-atom collisions.[1] In this model, the target and projectile atomic K orbitals combine in near-symmetric collisions forming the $2p\sigma$ and $1s\sigma$ diatomic molecular orbitals from which electrons are excited, and the resulting vacancies correlate to the projectile or target K shells or are shared between the two K shells according to the relative asymmetry between the two collision partners. The resulting plots of projectile and target K-vacancy production cross sections (Fig. 1 for 2.4-MeV/amu Xe ions) show considerable structure, which has been successfully interpreted using this model.

Roughly speaking, the molecular model is valid if the ratio of the ion velocity to the separated-atom projectile (Z_p) or target (Z_t) K-electron velocity $v/v_K=\beta/Z\alpha$ is less than approximately unity, where $\beta=v/c$, α is the fine-structure constant, and $Z=Z_t$ or Z_p. In the present papers, we report measurements where β ranges from 0.3 to 0.7 and $Z\alpha$ ranges from 0.2 to 0.8, so that velocity ratios close to or exceeding unity are used. Until now, no systematic studies of K-x-ray production in high-Z relativistic heavy-ion—atom collisions have been done. Only a few studies of target K-vacancy production using 160-MeV protons,[2] 4.88-GeV protons,[3] and 250-MeV/amu C ions[4] have been made.

A preview of the results, shown in Fig. 2 for 197-MeV/amu Xe ions, indicates that the structures seen in the low-velocity measurements are completely absent at these high energies. Interpretation with the molecular model is no longer possible, so we turn our attention to atomic models of inner-shell vacancy production. The

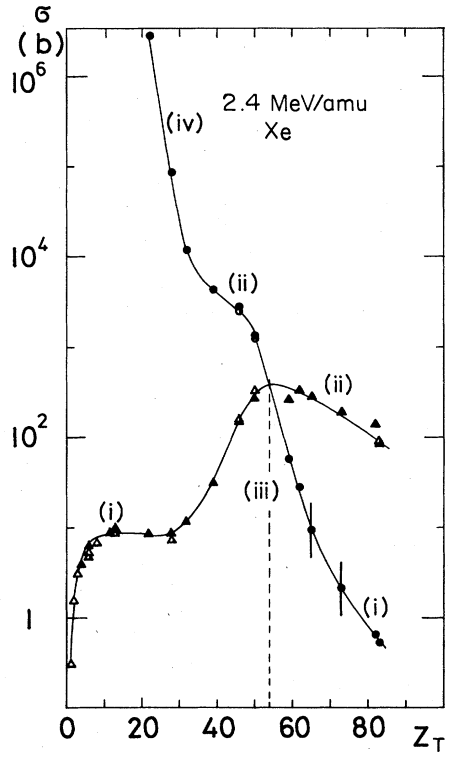

FIG. 1. Projectile (▲ and △) and target (●) K-vacancy production cross sections in 2.4-MeV/amu Xe collisions (Ref. 1). In these low-velocity collisions, electrons are excited from diatomic $1s\sigma$ and $2p\sigma$ molecular orbitals during the collision. $1s\sigma$ vacancy production is seen in regions (i), and $2p\sigma$ vacancy production is seen in regions (ii). The $2p\sigma$ vacancies are shared between the heavier and lighter collision partners in region (iii). Contributions due to $3d\sigma$ vacancy sharing are seen in region (iv). Dashed vertical line indicates symmetric collisions.

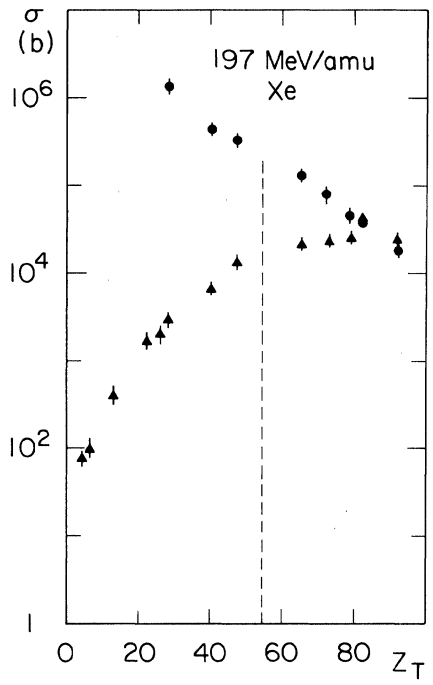

FIG. 2. Target K-vacancy (●) and projectile K-x-ray (▲) production cross sections in 197-MeV/amu collisions. The structures due to molecular excitation, seen in Fig. 1, are entirely absent in these collisions.

target K-vacancy production cross sections can be predicted using the plane-wave Born approximation, and atomic $1s$ and continuum wave functions.[4–7] Binding[8] and polarization effects,[9] which are understandable in the molecular model,[10] have only a minor influence on these cross sections, despite the fact that the relative atomic numbers used exceed the theoretical limitations of these theories. Projectile K-x-ray production is more difficult to interpret since the projectile can be nearly fully stripped in these collisions. Atomic theories of $1s$-$2p$ excitation, electron capture, and projectile K-shell ionization are used to interpret these data in a later paper in this series.

The present paper outlines the experimental methods used and examines target K-vacancy production. One motivation for these studies is the possible application of high-energy heavy ions to spark D-T fusion reactions.[11] Related questions of importance concern the stopping power (heat release) of high-Z heavy ions in matter and the relative amount of energy released by x rays, which can cause destructive preheating in high-gain fusion targets. As target K-vacancy production not only results in x-ray emission, but is a contribution to the total stopping power of an ion, the present studies bear on both of these topics. Few stopping powers for relativistic heavy ions have been measured. If disagreement with the atomic stopping-power theories occurs, the most affected contribution is liable to be from the innermost shell.

Another paper of this series considers other radiative processes seen in relativistic heavy-ion—atom collisions: radiative electron capture, secondary electron bremsstrahlung, and primary bremsstrahlung. Only a few, nonsystematic, studies of these processes were possible at low projectile energies, because the continua are relatively less intense, though they interfere with molecular orbital x-ray continuum measurements at low ion velocities.[12]

A further paper considers projectile K-x-ray formation. This is the most complicated subject because projectile K-x-ray formation requires a knowledge of projectile ionization, $1s$-$2p$ and $1s$-$3p$ excitation, and radiative and nonradiative electron capture. Among these, the least well understood process is nonradiative capture. The solution of time-dependent differential equations for the gain and loss of projectile electrons as the ion moves through solid targets, and the simultaneous production of projectile K x rays and radiative-capture photons, gives direct information on the charge state of the projectile in matter. Usually only ground-state-configuration gross projectile charge states are obtainable by magnetic charge-state analysis behind the targets, as discussed in another paper. Some of the arguments used in this series of papers are circular. The evidence derived from this paper points to the validity of using atomic ionization cross sections in part to derive the charge states of the projectile inside the target. However, target K vacancies can also be made by the capture of electrons into empty projectile K and L shells. After obtaining the projectile charge states, we return to the subject of target K-vacancy production.

II. EXPERIMENT

The counting apparatus used has evolved during the course of these measurements and, consequently, the relative experimental uncertainties have decreased. Two limitations of the Lawrence-Berkeley-Laboratory BEVALAC should be realized: (1) small beam currents ($< 10^5$ particles per sec, and typically $\sim 10^4$ per second) are obtainable, and (2) the beam is not well focused and cannot be collimated except for the heaviest ions at the smallest velocities. Attempted collimation generally leads to projectile fragmentation in the edges of the collimator, which leads to a shower of unstoppable lighter ions.

Consequently, we employed an "electronic collimation" method. The apparatus, shown in Fig. 3, counted coincidences between x rays and particles seen in two aligned, thin (< 800 μm) transmission mounted silicon surface-barrier particle detectors placed on either side of or both behind the target. A required triple coincidence assured that the x rays were emitted from a $\sim$2-cm-diam spot in the middle of the target; x rays coming from stray particles missing one or both particle detectors were not counted; particles not hitting both detectors could not make coincident x rays nor be counted in a scaler. Therefore, in this apparatus there is no uncertainty in the particle number normalization. The coincidence counting was done with standard fast-slow timing techniques. A generated gate signal from the time-to-amplitude convertor when the x rays and particles were in coincidence allowed x rays from a 75-mm^2 Si(Li) detector (for low-energy x rays) or a 1000-mm^2 Ge(i) detector (for high-energy x rays) to be counted in a multichannel analyzer or PDP 11/45 computer. Since a broad band of x rays was measured and the

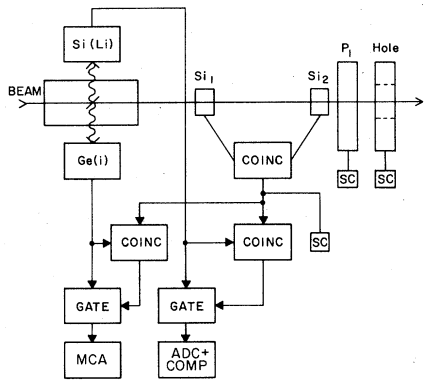

FIG. 3. Simplified schematic diagram of the experimental apparatus. Abbreviations: coincidence (COINC), multichannel analyzer (MCA), analog-to-digital convertor (ADC), computer (COMP), and scalers (SC).

true-to-random-coincidence ratio was enormous, no attempt was made to improve the ~100-nsec full width at half maximum (FWHM) timing resolution. Although the x-ray and γ-ray room background in the BEVALAC experimental areas was ~50 Hz, the particle coincidence condition eliminated virtually all room background. Several other downstream, thin, large-area (~50 cm^2), plastic-scintillator detectors, one with a hole approximately equal in size to the silicon detectors and aligned with them, were used to monitor the beam-focus quality. An excellent beam focus (never achieved) is one in which the number of silicon-detector coincidences is equal to the counts in the plastic detector, and the hole detector shows zero particles.

Self-supporting ~30-cm^2 metal foil targets with thicknesses between 5 and 100 mg/cm^2 were used. The use of these thicknesses assures that the projectile has an equilibrium charge state on the average, the projectile energy loss in the target is negligible, and reasonably quick measurements with the low beam current obtained from the BEVALAC could be done. Unfortunately, with these relatively thick targets, pileup effects and secondary target interactions are present, which are discussed in Sec. III.

The counting dead-time factor $D=p_{\text{in}}/p_c$ was monitored by triggering a number of pulses (p_{in}) into the x-ray detectors in proportion to the particle counting rate and comparing with the number counted (p_c) in the multichannel analyzer or computer.

The x-ray cross section is obtained from the x-ray yield per projectile Y_x using

$$\sigma_x(E_x)=\frac{Y_x}{n_2 TL} , \tag{1}$$

where n_2 is the target-atom density, T is the target thickness traversed by the projectile, L accounts for the x-ray self-absorption factor in the target tilted at 45°, with the x-ray detector at 90° from the beam axis,

$$L=\frac{1}{\mu(E_x)T}\{1-\exp[-\mu(E_x)T]\} , \tag{2}$$

and μ is the x-ray attenuation factor for the x ray of energy E_x in the target material.[13] The x-ray yield is given by

$$Y_x=\left[\frac{\text{counts in the peak}}{\text{coincident particles}}\right]\frac{D}{\epsilon\Omega_x} , \tag{3}$$

where $\epsilon\Omega_x$ is the efficiency and geometrical solid angle (fraction of 4π sr) subtended by the relevant x-ray detector. This quantity was measured with radioactive sources with the detector in place and includes the attenuation by the chamber window (250-μm Mylar), air, and an Al absorber (500 μm) on the Ge(i) detector.

Careful studies were made of the experimental uncertainties associated with this counting technique. To test whether the dead-time correction works properly, we measured Ag K-x-ray production in 197-MeV/amu Xe + Ag collisions, varying the BEVALAC particle current to obtain dead-time corrections D between 1.05 and 2.5. The resulting cross sections were equal to within ±2.7% [Fig. 4(a)]. We also assured that the measured cross sections are insensitive to the quality of the beam focus. The obtained reproducibility uncertainty, ±5% in Fig. 4(b), shows no correlation with the beam-focus quality, measured by the ratio of the number of counts on the hole detector to the number of Si-particle-detector coincidences. Further checks were obtained by comparing cross sections measured with the Ge(i) and Si(Li) detectors where overlap occurred ($40<Z_t<70$). Earlier measurements using Kr and Ne ions (and two rejected 120- and 190-MeV/amu Xe measurements) showed poorer

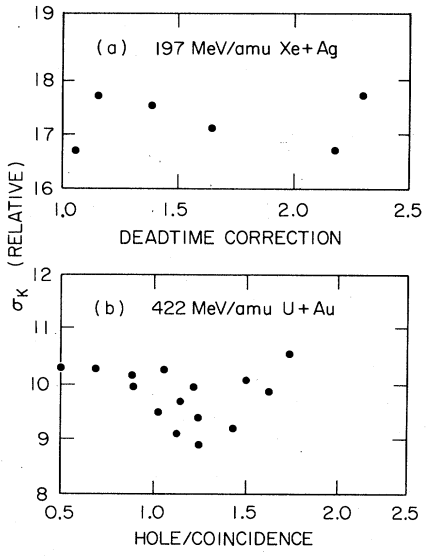

FIG. 4. Relative target K-x-ray cross sections measured in 197-MeV/amu Xe + Ag and 422-MeV/amu U + Au collisions. In (a) the particle rate was varied to obtain dead-time correction factors between 1.05 and 2.5. The cross sections are nearly independent of the dead-time correction, giving an average value 17.2±0.46 (±2.7%). In (b), the beam focus, measured by the relative number of particles counted by the plastic-scintillator detector with a hole aligned with the particle detectors, was varied, and the resulting cross sections are also approximately equal, within a standard deviation of ±5%.

TABLE I. Experimental uncertainties. Experiment I: 425-MeV/amu Kr, 670-MeV/amu Ne. Experiment II: 82- and 197-MeV/amu Xe, 175-MeV/amu La, and 422-MeV/amu U.

	Expt. I	Expt. II	Appearing in $\sigma_t(Z_t)$	$\sigma_p(Z_t)$	$d\sigma/d\Omega$	$\sigma_t(T)$
Reproducibility	±30[b]	±5	yes	yes	yes	yes
Target angle	±8	±2.5	yes	yes	no	yes
Target thickness	±3	±3	yes	yes	no	yes
Detector efficiency	±10	±10	yes	yes	±3	no
Statistics, background	variable		neg.	yes	yes	neg.
Net (except statistics)	Expt. I:		±32	±32	a	±30
	Expt. II:		±12	±12	±6	±6.3

[a] Not done.
[b] All numbers in percent.

reproducibility, possibly due to inferior electronic hardware.

Other uncertainties included that in the target thickness, obtained by weighing $\sim$30-cm^2 targets, and measuring the corresponding area. The target thickness uniformity is not known, but since a large fraction ($\sim$30%) of the target area was used, we assume no uncertainty in the uniformity. The uncertainty in the target angle with respect to the beam axis, measured by reflecting laser light from stainless-steel targets placed on the target holder in later measurements, was approximately ±1.5°, giving an additional ±2.5% uncertainty in the target thickness or cross section. The uncertainty in the detector efficiency and geometry calibration is approximately ±10%. The statistical uncertainties are negligible for measurements of target K x rays where the x-ray continuum background is relatively smaller. For the weaker projectile K x rays and the radiative-electron-capture photons, these errors were more significant. Table I summarizes these uncertainties for experiments I (using Ne and Kr ions) and II (using Xe, La, and U ions). In this series of papers, four kinds of measurements are described: measurements of the Z_t dependence of target $[\sigma(Z_t)]$ and projectile $[\sigma(Z_p)]$ K x rays, K vacancies, radiative-capture photons, or continua; relative measurements of x-ray and radiative-capture-photon angular distributions $d\sigma/d\Omega$ (where the uncertainty in the fixed target angle and thickness is unimportant, and where the detector efficiency and geometry is known relatively to ±3%); and relative measurements of the target thickness dependence $[\sigma_t(T)]$ (where detector efficiency and geometry uncertainties are unimportant). The net uncertainties in these measurements, excluding statistical ones, are also given in Table I.

III. CORRECTIONS TO TARGET K-VACANCY PRODUCTION

A. x-ray pileup

Figure 5 shows an x-ray spectrum seen in 197-MeV/amu Xe + Tb collisions. Besides the Xe $K\alpha$ and Tb $K\alpha$ and $K\beta$ x rays and a steeply falling continuum spectrum (discussed in a later paper), sharp lines due to the electronic pileup of two target $K\alpha$ x rays or a $K\alpha$ and a $K\beta$ x ray are seen. The origin of this electronic pileup at peak beam particle rates of $<10^4$ Hz at first was difficult to comprehend. Measurements showed that the ratio of the intensity of the pileup peaks to the $K\alpha$ peak is independent of the beam current as it varied by a factor of 10 [Fig. 6(b)]. The ratio is proportional to the target thickness, however [Fig. 6(a)].

It should be realized that a single 197-MeV/amu Xe ion in a $\sim$70-mg/cm^2 target creates $\sim$70 Ag K x rays. With a detection efficiency $\epsilon\Omega_x \approx 10^{-3}$, we detect a fractional yield P equal to 0.07 photons per projectile. The probability of two photons simultaneously striking the x-ray detector and giving a pileup peak is P^2. The expected ratio of the peak areas is therefore $P^2/P = 0.07$. The number of photons per projectile P and hence the pileup peak ratio increases linearly with T until the self-absorption

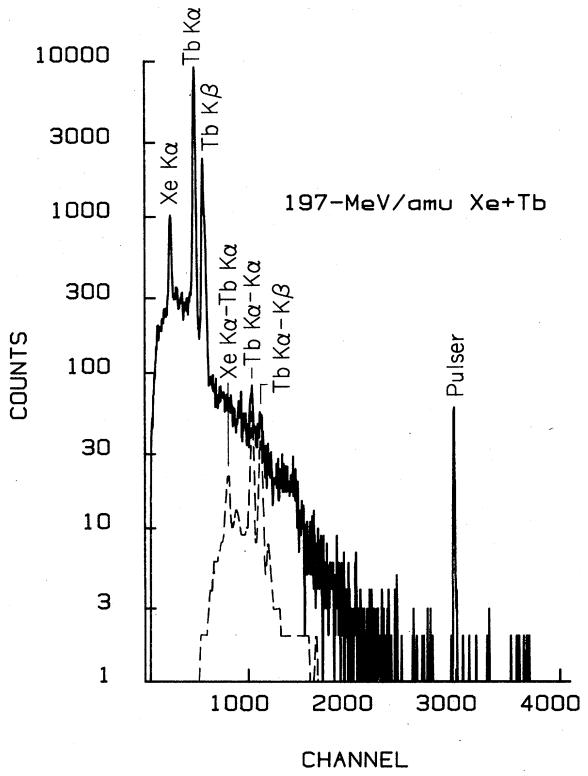

FIG. 5. An x-ray spectrum for 197-MeV/amu Xe + Tb collisions and the calculated pileup spectrum (dashed line).

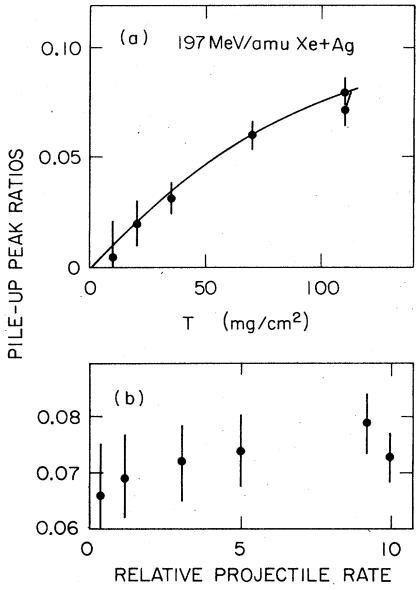

FIG. 6. Ratios of the intensity of the target $K\alpha$-$K\alpha$ and $K\alpha$-$K\beta$ pileup peaks to the target $K\alpha$ x-ray intensity versus target thickness (a) and the relative projectile rate (b).

factor L in Eq. (2) becomes significantly less than unity, as shown in Fig. 6(a). Since each projectile has the same probability for producing this pileup, the pileup peak ratio is independent of beam current, as shown in Fig. 6(b). The pileup rejectors used with the x-ray detectors have no effect on the pileup peak intensity since they cannot resolve x rays arriving less than 100 nsec apart, and the photons originating from the same projectile arrive less than one psec apart.

To correct for this pileup we could add the pileup peak counts to the $K\alpha$ counts, but this only corrects for the target $K\alpha$-$K\alpha$ and $K\alpha$-$K\beta$ pileup. The $K\alpha$ photons pileup on continuum and other photons also (giving the estimated dashed curves in Fig. 5 as described in a later paper). The total probability of detecting an x ray for every projectile is

$$P_{\text{tot}} = \int_0^\infty dE_x n_2 \frac{d\sigma}{dE_x} LT\epsilon\Omega_x \,, \tag{4}$$

which is approximately equal to the total number of dead-time-corrected counts in the x-ray spectrum divided by the total number of particles. The probability of detecting a $K\alpha$ x ray without pileup is

$$P'_\alpha = P_\alpha(1-P_{\text{tot}}) \,, \tag{5}$$

where the quantity we wish to obtain is the total number of $K\alpha$ x rays proportional to P_α instead of the number showing no pileup, proportional to P'_α. Division of P'_α by $1-P_{\text{tot}}$ gives the desired quantity.

We evaluated expression (4) by using the measured probability P'_{tot} instead of P_{tot}. The quantity P'_{tot} contains some events where two photons are counted as one. The difference between P_{tot} and P'_{tot} is small, however, and since the net correction $1-P'_{\text{tot}}$ is greater than 0.9, no large errors are incurred in this approximation.

These corrections are seen in the target-thickness dependence of Ag and Ta K x-ray production in Fig. 7. The measured cross sections, proportional to P'_α, appear to decrease with target thickness. Addition of the individual pileup peaks to the Ag $K\alpha$ intensity gives a nearly target-thickness-independent cross section. Correction using the total emission probability gives a cross section that increases with target thickness.

These pileup corrections were made for all of the data presented in this series of papers, since it likewise affects projectile K-x-ray and REC cross sections. In general, however, the corrections are negligible in collisions with low projectile atomic number (e.g., Ne collisions) and low target atomic number.

B. Secondary target interactions

Target K-shell ionization can occur as the result of secondary and tertiary processes,[2,3] shown in Fig. 8. A $\sim$200-MeV/amu heavy ion can elastically scatter any target electron in a binary encounter, producing ionized electrons with kinetic energies up to $E_{\text{max}}=400$ keV. These electrons can ionize K-shell electrons in other nearby target atoms (process 1) or they can emit bremsstrahlung photons in secondary collisions with other target atoms which can be absorbed photoelectrically in still other target-atom K shells (process 2).

The relative cross section for process 1 is given by

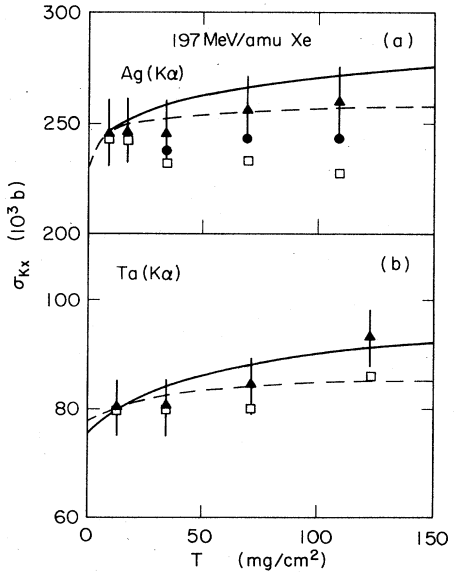

FIG. 7. Target-thickness dependence of Ag and Ta $K\alpha$ x-ray production in 197-MeV/amu Xe collisions. Corrections to the original data (□) were made by adding the intensity of the discreet $K\alpha$-$K\alpha$ and $K\alpha$-$K\beta$ pileup peaks (●), or multiplying by $(1-P'_{\text{tot}})^{-1}$ as in Eq. (5) (▲). The calculated target-thickness dependences for process (1) (dashed line) and for processes 1 and 2 (solid line) are shown.

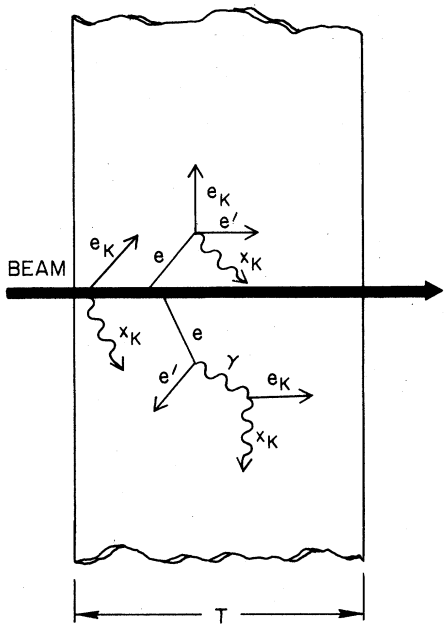

FIG. 8. Primary and secondary processes 1 and 2 for producing target K vacancies.

$$\frac{\Delta\sigma'_K}{\sigma_K}=\frac{Z_t}{\sigma_K(Z_p)}\int_{U_K}^{E_{\max}}dE_e\int_0^{2\pi}d\phi\frac{d^2\sigma_{\rm elas}}{dE_e d\phi}\times\int_0^T\frac{dx}{T}\int_{E_e}^{F}-\frac{dE'_e}{S(E'_e)}n_2\sigma_K(E'_e)\,, \tag{6}$$

where $S(E'_e)$ is the stopping power of the electron in the target given by the Bethe formula[14]

$$S(E_e)=\frac{4\pi e^4 n_2}{mc^2\beta_e^2}Z_t\left[\ln\frac{2\gamma_e^2\beta_e^2mc^2}{\langle I\rangle}-\beta_e^2\right], \tag{7}$$

β_e is the relative electron velocity, $\gamma_e=1+E_e/mc^2$, $\langle I\rangle$ is the average ionization potential,[14] F is the smaller value of the K-shell binding energy or the energy of the electron emerging from the target through a thickness T_r given by[15]

$$T_r=(T-x)\frac{\sec\theta_r\tan\theta_T}{|\tan\theta_T-\tan\theta_r\cos\phi|}\,, \tag{8}$$

θ_T is the target angle, θ_r is the electron recoil angle classically related to its energy by

$$E_e=E_{\max}\cos^2\theta_r\,, \tag{9}$$

$E_{\max}=2\gamma^2\beta^2mc^2$, and γ and β are the projectile relativistic energy and velocity parameters. For pure elastic scattering in the binary projectile-electron encounter, the elastic scattering cross section neglecting McKinley-Feshbach terms[16] is given by

$$\frac{d\sigma_{\rm elas}}{dE_e d\phi}=\frac{(Z_p e^2)^2}{mc^2\beta^2}\frac{1}{E_e^2} \tag{10}$$

for $E_e<E_{\max}$. For the K-shell ionization cross section for electrons $\sigma_K(E_e)$ and the projectile $\sigma_K(Z_p)$, we use the Bethe approximation discussed in Sec. IV.

The evaluation of the quadruple integral in Eq. (6) is tedious, but relatively precise. Errors incurred by using the approximate Bethe cross section for K-shell ionization should cancel out. Incorporation of the Fermi motion of the target electrons into the elastic cross section should have little effect at these high energies. The relative corrections $\Delta\sigma'_K/\sigma_K$ are less than ~ 0.2 which is not much greater than the experimental uncertainties. For infinitely thick targets (F is always equal to U_K), an approximate analytical formula can be derived which agrees well with our numerical results.

The cross section for process 2 is more difficult to evaluate precisely. Assuming that all bremsstrahlung photons are emitted in the forward direction (parallel to $\vec{\beta}_e$) we have

$$\frac{\Delta\sigma''_K}{\sigma_K}=\frac{Z_t}{\sigma_K(Z_p)}\int_{U_K}^{E_{\max}}dE_e\int_0^{2\pi}d\phi\frac{d^2\sigma_{\rm elas}}{dE_e d\phi}\times\int_0^T\frac{dx}{T}\int_{E_e}^{F}-\frac{dE'_e}{S(E'_e)}n_2\int_{U_K}^{E'_e}dE_x\frac{d\sigma_{\rm brem}}{dE_x}\frac{\mu_K(E_x)}{\mu_{\rm tot}(E_x)}\times(1-\exp\{-\mu_{\rm tot}(E_x)[T_r-T_e(E'_e)]\})\,, \tag{11}$$

where the bremsstrahlung cross section is given by the Bethe-Heitler formula with the Elwert correction factor[17,18] and μ_K and $\mu_{\rm tot}$ are the K-shell and total photoelectric absorption cross sections[13] for the photon of energy E_x emitted through the remaining target distance $T_r-T_e(E'_e)$, where T_e is the distance the electron travels before bremsstrahlung scattering. This equation is not only less precise than Eq. (6) because of the uncertainty in the remaining distance the photon travels, but because the uncertainty in the K-shell ionization cross section does not cancel out.

Figure 9 shows calculations of the relative corrections for 200-MeV/amu ions on several different targets. The bremsstrahlung process is most important in high-Z targets. The relative cross section for process 2 increases faster with target thickness at low thickness, and reaches saturation (the infinite-target-thickness value) at lower thicknesses in low-Z targets and higher ones in high-Z targets. These dependences are also seen in Fig. 7 for 197-MeV/amu Xe + Ag and Xe + Ta collisions where the relative corrections are normalized at the smallest target thickness. Most of the targets used in this work were near the saturation thickness; the steepest rise in the dependence is below the lowest thickness in Ag and below

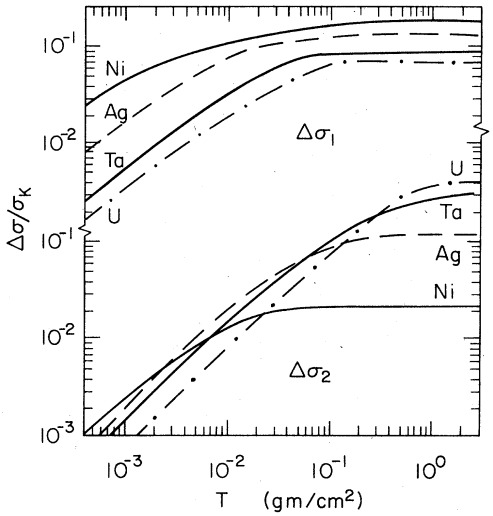

FIG. 9. Calculated relative increase in the target K-vacancy production cross sections with the target thickness traversed by the beam for processes 1 and 2 in 197-MeV/amu collisions.

at least the two lowest thicknesses in Ta. We hoped to calibrate the accuracy of the correction factor for process 2 using the experimental data, but the relatively large experimental uncertainties prevented this. For Ag, the data and calculations agree best where process 2 is neglected. Only one point in Ta supports the magnitude of the correction factor for process 2.

The quantities we wish to extract are the cross section at zero target thickness given by

$$\sigma_{Kx}=\sigma'_{Kx}(1-P'_{\rm tot})^{-1}\left[1+\frac{\Delta\sigma'_K(T)+\Delta\sigma''_K(T)}{\sigma_K}\right]^{-1}. \tag{12}$$

The difference between the cross sections calculated with and without process 2 is negligible compared with the relative experimental uncertainties in Fig. 9, and even more negligible with respect to the larger absolute uncertainties.

IV. THEORIES OF TARGET K-VACANCY PRODUCTION

In the plane-wave Born approximation, the K-shell ionization cross section per electron is given by[7,19]

$$\sigma_K=\frac{8\pi(Z_pe^2)^2}{mc^2\beta^2}\int_0^\infty d\epsilon \times\int_{q_{\rm min}}^{q_{\rm max}} q\,dq\left[\frac{|F_\epsilon(q)|^2}{q^4}+\frac{\beta^2(1-q^2_{\rm min}/q^2)\,|\vec{\rm G}_\epsilon|^2}{(q^2-q^2_{\rm min}\beta^2)^2}\right], \tag{13}$$

where ϵ is the kinetic energy of the ionized electron, $q_{\rm min}=(U_K+\epsilon)/\beta c$ is the minimum momentum transfer, U_K is the K-shell binding energy, $q_{\rm max}=2\gamma\beta mc$ is the maximum momentum transfer to the electron, $F_\epsilon(q)$ and $\vec{\rm G}_\epsilon(q)$ are matrix elements given by

$$F_\epsilon(q)=\langle\phi_\epsilon|\,e^{i\vec{q}\cdot\vec{r}}\,|\phi_{1s}\rangle\,,$$
$$\vec{\rm G}_\epsilon(q)=\langle\phi_\epsilon|\,\vec{\alpha}e^{i\vec{q}\cdot\vec{r}}\,|\phi_{1s}\rangle\,, \tag{14}$$

$\vec{\alpha}$ is the Dirac matrix operator, and ϕ_ϵ and ϕ_{1s} are target-atom continuum and $1s$ wave functions. Evaluation of these equations has been done by Khandelwal *et al.*[6] and Rice *et al.*[20] for the longitudinal term involving F_ϵ and by Anholt [Eq. (24) of Ref. 7] for the transverse term involving $\vec{\rm G}_\epsilon$.

For the relatively high projectile velocities used in this work, it is possible to use a version of the Bethe approximation to calculate K-shell ionization cross sections. Since the approximate magnitude of $\vec{q}\cdot\vec{r}$ in the longitudinal and transverse matrix elements is smaller than unity on the average, we can use

$$F_\epsilon(q)\approx i\vec{q}\cdot\langle\phi_\epsilon|\,\vec{r}\,|\phi_{1s}\rangle\,,$$
and
$$\vec{\rm G}_\epsilon\approx\langle\phi_\epsilon|\,\vec{\alpha}\,|\phi_{1s}\rangle=iq_{\rm min}\beta\langle\phi_\epsilon|\,\vec{r}\,|\phi_{1s}\rangle\,. \tag{15}$$

Then, setting $q_{\rm min}=U_K/\beta c$ and $q_{\rm max}=\sqrt{2U_K}$, we obtain[19]

$$\sigma_K=\frac{4\pi(Z_pe^2)^2}{mc^2\beta^2}\int_0^\infty d\epsilon\,|\langle\phi_\epsilon|\,\vec{r}\,|\phi_{1s}\rangle|^2\times\left[\ln\frac{2mc^2\gamma^2\beta^2}{U_K}-\beta^2\right]. \tag{16}$$

In theories of electronic stopping power the sum over excited states (integral over ϵ) contains the energy loss $U_K+\epsilon$ for each state which, combined with the squared dipole transition matrix element, is the oscillator strength that sums or integrates to unity.[19] For the K-shell cross sections, we cannot use this convenient fact. Instead we relate the dipole matrix element to the K-shell photoelectric cross section using

$$\sigma_{K\rm PE}=(2\pi)^2\alpha(U_K+\epsilon)\,|\langle\phi_\epsilon|\,\vec{r}\,|\phi_{1s}\rangle|^2\,. \tag{17}$$

Since $\sigma_{K\rm PE}$ varies as

$$\sigma_{K\rm PE}=\sigma_{K\rm PE}(U_K)\left[\frac{U_K}{U_K+\epsilon}\right]^n, \tag{18}$$

the integral over ϵ is easily done, so we obtain

$$\sigma_K=\frac{4\pi(Z_p\alpha)^2}{\beta^2}\frac{\sigma_{K\rm PE}(U_K)}{(2\pi)^2\alpha n}\times\left[\ln\frac{2mc^2\gamma^2\beta^2}{U_K}-\beta^2\right]. \tag{19}$$

The photoelectric cross section and slope (n) can be obtained from a number of tables[13] based on experimental values or relativistic Hartree-Fock wave functions. This cross section was used to calculate the target-thickness correction factors in Eqs. (6)—(11).

The plane-wave Born and Bethe theories neglect the distortion of the target electronic wave functions due to the presence of the high-Z projectile. At low projectile velocities, the inner-shell electrons have sufficient time during the collision to form molecular orbitals. The most

important molecular effect is the increased binding of the K electron correlating to the heavier collision partner, making it more difficult to excite, and giving smaller ionization cross sections than those predicted using the atomic theories.[8,10] At high velocities where molecular orbitals are not formed, a "polarization" effect is present.[9] One interpretation of this polarization is that the target electron clouds stretch toward the projectile nucleus in large impact-parameter collisions, bringing the projectile and electron closer together, which increases the excitation cross section. In detailed multichannel calculations of K-shell ionization, this polarization is seen in the population of side excitation pathways; instead of the direct excitation of $1s$ electrons to p continuum states, excitation to s and d states followed by s to p and d to p transitions are possible.[21] Since the direct-excitation amplitudes are proportional to the projectile atomic charge Z_p, and the two-step amplitudes are proportional to Z_p^2, the excitation probability is proportional to a term in Z_p^2 and a second term in Z_p^3 (plus higher-order terms). The population of s and d states can be interpreted as polarization of the electron clouds.

Theories of the binding effect on K-shell ionization at low velocities and the polarization effect on stopping powers and K-shell ionization at higher velocities have been formulated.[8,9] Basbas *et al.*[22] developed a formulation that interpolates between the low- and high-velocity regimes, which is precisely the velocity region of interest in this work. The theories assume that $Z_p \ll Z_t$, however, and we have $Z_p > Z_t$ in some cases. Nevertheless, we compare with these theories in Fig. 10. Also, the effect on the transverse term has not been formulated, so we apply the binding-polarization correction to both the longitudinal and transverse terms equally (the transverse term being much smaller than the longitudinal in this work, anyway).

One other correction usually applied to K-shell ionization cross sections is for electronic relativistic wave functions.[23,10] In deriving Eq. (13), partially relativistic Darwin electronic wave functions were used which have the four-component structure of fully relativistic wave functions, but lack the correct properties at high momentum transfer which are important in collisions with low-velocity ions.[23] These properties are not expected to be important at the velocities considered here. Some indication of this is found in the comparison of Bethe-approximation calculations of K-shell ionization using hydrogenic and relativistic Hartree-Fock wave functions to obtain the photoelectric cross section in Eq. (19). The two calculations differ by less than 10%, so the application of a relativistic wave-function correction to these theories is unnecessary.

V. RESULTS FOR K-SHELL IONIZATION

The remarkable conclusion of this work is that despite the very high projectile charges used and the not-exceedingly-high relative velocities, the data agree well with the atomic theories. The ratio of the projectile velocity to the K-electron velocity in Fig. 10 varies from 4 (670-MeV/amu Ne + Ni) to 1.2 (670-MeV/amu Ne + U) or 2 (82-MeV/amu Xe + Ni) to 0.6 (82-MeV/amu

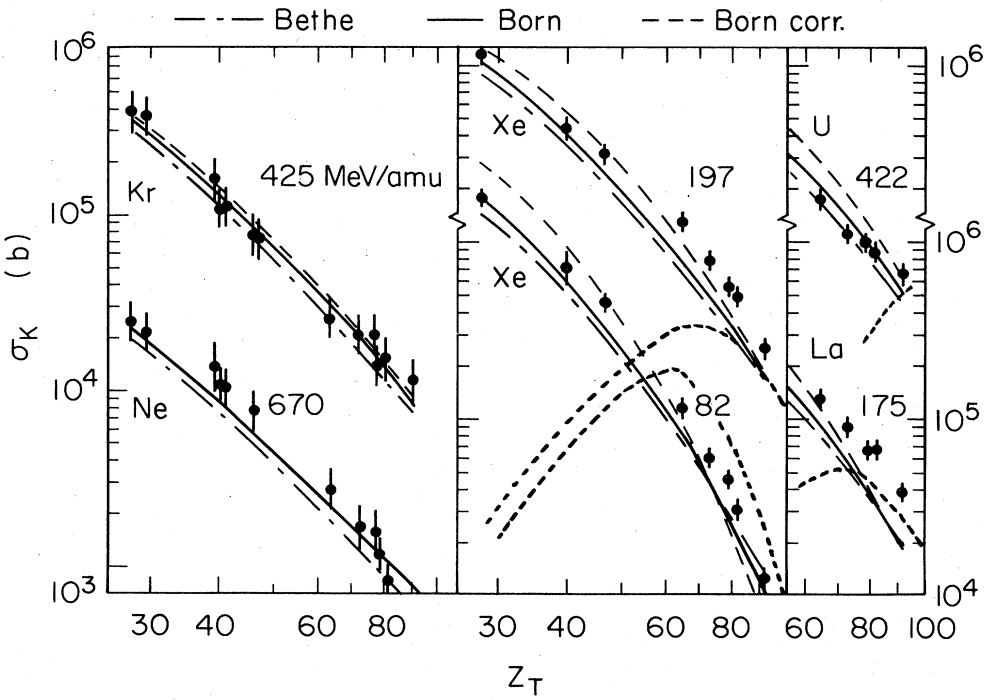

FIG. 10. K-shell vacancy production cross sections. The ionization cross sections were calculated with the atomic plane-wave Born approximation [Eq. (3); solid line], Bethe approximation [Eq. (19); chain curve], and the Born approximation with corrections for binding and polarization effects (long-dashed curve). Fully stripped projectiles can also capture target K electrons, giving the contributions shown by the short-dashed curves.

Xe + U). The Bethe and exact plane-wave Born approximation theories differ by approximately 30% for $v/v_K > 1$. The Bethe approximation is less valid for $v/v_K < 1$, and exceeds the exact Born-approximation results at those velocities. The polarization and binding corrections give larger cross sections for $v/v_K > 1$ and smaller ones for $v/v_K < 1$. They are negligibly small for Ne collisions and are as large as a factor of 1.8 in, e.g., Xe + Ni collisions. The data do not consistently support the application of these corrections: the experimental uncertainties are larger than the difference between the corrected and uncorrected theories in the Ne and Kr collisions, and the data points for $Z_t < 60$ in the Xe, La, and U collisions do not consistently agree better with either.

For high Z_t in Xe and La collisions, nonradiative capture of target K electrons by the projectile contributes to the observed K-vacancy production cross sections. The evaluation of the capture contribution requires a knowledge of the projectile charge states and the nonradiative capture cross sections. We defer the discussion of this to a later paper in this series. To indicate the relative variation of the capture contribution, we plot in Fig. 10 the Oppenheimer-Brinkmann-Kramers cross section (multiplied by the Drisko factor,[24] ~ 0.295) evaluated for relativistic ions by Moiseiwitsch and Stockman,[25] assuming the projectile is fully stripped. These calculations show that capture is responsible for the deviation between the measured and calculated ionization cross sections at large Z_t in Xe and La collisions, though the present capture cross sections are too large in places. In part, this is because we assumed the projectile is fully stripped, which is least valid for 82-MeV/amu Xe collisions where the calculated relative capture contributions are greatest. Capture is negligible with 670-MeV/amu Ne and 425-MeV/amu Kr projectiles.

VI. RESULTS FOR L-SHELL IONIZATION

Target $L\alpha$, $L\beta$, and $L\gamma$ x-ray production cross sections were measured for targets ranging from Ta to U. These x-ray lines are due to the filling of L_1, L_2, and L_3 vacancies, and the x-ray production cross sections σ_{Lx}, are calculated from the vacancy production cross sections σ_{Li} using

$$\sigma_{Lxi} = A_{Lxi1}\sigma_{L1} + A_{Lxi2}\sigma_{L2} + A_{Lxi3}\sigma_{L3} , \tag{20}$$

where the coefficients A_{Lxij} are given by a combination of measured or calculated L-shell fluorescence yields ω_{Li}, Coster-Kronig transition probabilities f_{ij}, and branching ratios Γ_{Lxi}/Γ_{Li} given in Table II.[26–28] The direct extraction of ionization cross sections σ_{Li} using methods based on the intensity of the weak $L\gamma_4$ line[29] proved impossible in this work due to the poor x-ray energy resolution and the intense continuum background.

The L x-ray cross sections are also thickness dependent due to secondary processes, and a correction factor based on the L_3 ionization cross section was calculated. Similar correction factors for L_1 and L_2 ionization are expected, so the ratio $\Delta\sigma_{L3}(T)/\sigma_{L3}$ can be applied directly to the L-x-ray cross sections, as shown in Fig. 11 for 197-MeV/amu Xe + Ta collisions.

The corrected zero-target-thickness cross sections are compared with atomic plane-wave Born calculations in Fig. 12. Although the longitudinal contribution to L-shell ionization can be calculated using the tabulations of Khandelwal *et al.*,[6] the formulation of the transverse contribution to L-shell ionization has not been done. In

TABLE II. L-shell x-ray production parameters. Parameters ω_1 through f_{23} from Refs. 27 ($Z_t = 70$ and 82) and 28 ($Z_t = 92$). The relative transition rates are from Ref. 26. Definitions: $A_{L\alpha 1} = (f_{13} + f_{12}f_{23})\omega_3\Gamma_{3\alpha}/\Gamma_3$, $A_{L\alpha 2} = f_{23}\omega_3\Gamma_{3\alpha}/\Gamma_3$, $A_{L\alpha 3} = \omega_3\Gamma_{3\alpha}/\Gamma_3$, $A_{L\beta 1} = (f_{13} + f_{12}f_{23})\omega_3\Gamma_{3\beta}/\Gamma_3 + f_{12}\omega_2\Gamma_{2\beta}/\Gamma_2 + \omega_1\Gamma_{1\beta}/\Gamma_1$, $A_{L\beta 2} = f_{23}\omega_3\Gamma_{3\beta}/\Gamma_3 + \omega_2\Gamma_{2\beta}/\Gamma_2$, $A_{L\beta 3} = \omega_3\Gamma_{3\beta}/\Gamma_3$, $A_{L\gamma 1} = f_{12}\omega_2\Gamma_{2\gamma}/\Gamma_2 + \omega_1\Gamma_{1\gamma}/\Gamma_1$, $A_{L\gamma 2} = \omega_2\Gamma_{2\gamma}/\Gamma_2$, $A_{L\gamma 3} = 0$.

Parameter	$Z_t = 70$	$Z_t = 82$	$Z_t = 92$
ω_1	0.113	0.116	0.215
ω_2	0.239	0.402	0.56
ω_3	0.23	0.374	0.49
f_{12}	0.199	0.072	0.069
f_{13}	0.319	0.653	0.55
f_{23}	0.132	0.109	0.23
$\Gamma_{3\alpha}/\Gamma_3$	0.845	0.79	0.76
$\Gamma_{2\beta}/\Gamma_2$	0.835	0.78	0.754
$\Gamma_{1\beta}/\Gamma_1$	0.77	0.74	0.714
$A_{L\alpha 1}$	0.067 05	0.195	0.211
$A_{L\alpha 2}$	0.0257	0.032	0.0857
$A_{L\alpha 3}$	0.184	0.296	0.372
$A_{L\beta 1}$	0.139	0.161	0.248
$A_{L\beta 2}$	0.201	0.322	0.448
$A_{L\beta 3}$	0.0359	0.0797	0.116
$A_{L\gamma 1}$	0.0338	0.0365	0.0712
$A_{L\gamma 2}$	0.0394	0.0884	0.14

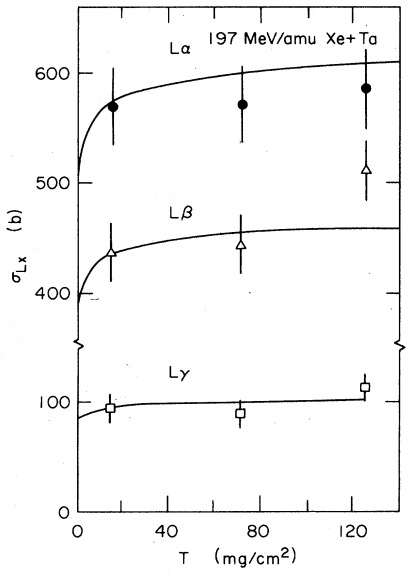

FIG. 11. The target-thickness dependence of Ta $L\alpha$, $L\beta$, and $L\gamma$ x-ray production in 197-MeV/amu Xe + Ta collisions. The calculated dependence (solid line) includes processes 1 and 2.

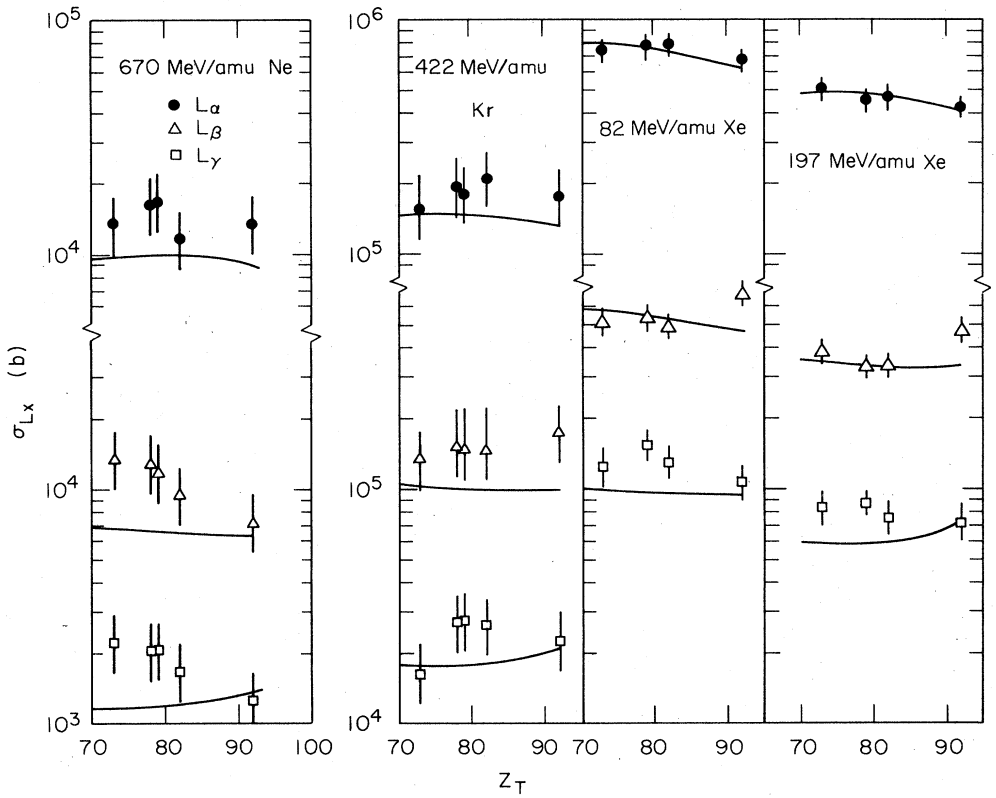

FIG. 12. Target $L\alpha$, $L\beta$, and $L\gamma$ x-ray production for several projectiles. Solid line shows the plane-wave Born-approximation ionization cross sections converted to x-ray cross sections using single-vacancy fluorescence yields and Koster-Kronig transition probabilities.

the dipole approximation, the ratio of the total to the longitudinal cross sections are given by

$$\frac{\sigma_{\text{tot}}}{\sigma_{\text{long}}} = 1 + \frac{\ln\gamma^2 - \beta^2}{\ln(E_{\max}/U\gamma^2)} , \tag{21}$$

where $E_{\max} = 2mc^2\gamma^2\beta^2$ and U is the relevant electron binding energy. The L_3 correction factor is largest in 670-MeV/amu Ne collisions, where it varies from 1.10 to 1.11 between $Z_t = 70$ and 92. In view of its small magnitude, a complete evaluation of the transverse L-shell cross section is not required here; the longitudinal cross sections were multiplied by these ratios.

The measured and calculated L-x-ray cross sections agree well, especially for $L\alpha$ and $L\beta$ x-ray production by Xe ions. The $L\gamma$ cross sections are higher than the calculations everywhere, possibly due to uncertainties in the fluorescence yields. The difference between theory and experiment for the Ne and Kr cross sections lies outside of the experimental uncertainties. Arguing from similar electron binding energies, polarization, binding, and capture effects in these collisions are likely to be as significant as the effects on K-shell ionization in targets between $Z_t = 30$ and 47. As shown in Fig. 10, capture contributions should be negligible. Estimated polarization and binding corrections would increase the Xe cross sections by up to a factor of 1.8, the Kr cross sections by a factor of ~ 1.3, and the Ne cross sections negligibly. The data do not support the application of such corrections.

VII. CONCLUSIONS

Target K-vacancy and L-x-ray cross sections induced by relativistic high-Z heavy ions can be predicted within less than a factor of 2 by atomic theories of inner-shell ionization. Structure in the Z_t dependence of these cross sections, seen in low-velocity collisions as the result of molecular effects, is essentially absent. Since K- and L-shell ionization contribute to electron stopping powers of relativistic heavy ions in matter, this work suggests that the atomic theories of electronic stopping should also be valid in these high-Z_t collisions. It is likely that deviations in electronic stopping powers due to electronic-wave-function-distortion effects appear more in the inner-shell contributions than in the dominant outer-shell contributions. Finally, the atomic theories can now provide an estimate for radiative preheating of inner shells of high-gain inertial fusion targets.[30]

ACKNOWLEDGMENTS

This work was supported in part by the National Science Foundation Grant No. PHY-83-13676, by the Department of Energy Contract No. DE-AC-03-76-SF-00098, by the Swiss National Fund (E.M.), and by a NATO postdoctoral fellowship (S.A.A.). W. McHarris and D. Spooner took part in some of the data taking. We thank H. Gould, F. Lothrup, and the crew of the Lawrence Berkeley Laboratory BEVALAC for advice or contributions of time and equipment. The data-acquisition system was tailored to these experiments by B. Neyer and J. Thornton.

*Permanent address: Laboratory for Medium Energy Physics, Eidgenössiche Technische Hochschule—Hönggerberg, Zurich, Switzerland.

†Permanent address: Centre d'Etudes Nucleaires, University of Bordeaux, Gradignan, France.

‡Permanent address: Department of Physics, Fudan University, Shanghai, People's Republic of China.

[1]W. E. Meyerhof, R. Anholt, T. K. Saylor, S. M. Lazarus, A. Little, and L. F. Chase, Jr., Phys. Rev. A **14**, 1653 (1976).

[2]O. N. Jarvis, C. Whitehead, and M. Shah, Phys. Rev. A **5**, 1198 (1972).

[3]R. Anholt, S. Nagamiya, H. Bowman, J. Ioannou, E. Rauscher, and J. O. Rasmussen, Phys. Rev. A **14**, 2103 (1976).

[4]R. Anholt, J. Ioannou, H. Bowman, E. Rauscher, S. Nagamiya, J. O. Rasmussen, T. Shibata, and H. Ejiri, Phys. Lett. **59A**, 429 (1977).

[5]E. Merzbacher and H. W. Lewis, in *Encyclopedia of Physics,* edited by S. Flügge (Springer, Berlin, 1958).

[6]G. W. Khandelwal, B. H. Choi, and E. Merzbacher, At. Data **1**, 103 (1969).

[7]R. Anholt, Phys. Rev. A **19**, 1009 (1979).

[8]G. Basbas, W. Brandt, and R. Laubert, Phys. Rev. A **7**, 983 (1973).

[9]G. Basbas, W. Brandt, and R. Laubert, Phys. Lett. **34A**, 277 (1971).

[10]R. Anholt and W. E. Meyerhof, Phys. Rev. A **16**, 190 (1977).

[11]D. Keefe, Annu. Rev. Nucl. Sci. **32**, 391 (1982).

[12]W. E. Meyerhof, Science **193**, 839 (1976).

[13]W. H. McMaster, N. Kerr del Grande, J. H. Mallett, and J. H. Hubbel, Lawrence Livermore Report No. UCRL-50174, 1969 (unpublished).

[14]S. Ahlen, Rev. Mod. Phys. **52**, 140 (1980).

[15]D. Burch and K. Taulbjerg, Phys. Rev. A **12**, 508 (1975).

[16]J. D. Jackson and R. L. McCarthy, Phys. Rev. B **6**, 4131 (1972).

[17]H. K. Tseng, R. H. Pratt, and C. M. Lee, Phys. Rev. A **19**, 187 (1979).

[18]H. K. Koch and J. W. Motz, Rev. Mod. Phys. **31**, 920 (1959).

[19]U. Fano, Annu. Rev. Nucl. Sci. **13**, 1 (1963).

[20]R. Rice, G. Basbas, and F. D. McDaniel, At. Data Nucl. Data Tables **20**, 503 (1977).

[21]K. W. Hill and E. Merzbacher, Phys. Rev. A **9**, 156 (1974).

[22]G. Basbas, W. Brandt, and R. Laubert, Phys. Rev. A **17**, 1655 (1978).

[23]P. A. Amundsen, L. Kocbach, and J. M. Hansteen, J. Phys. B **9**, L203 (1976).

[24]R. M. Drisko, thesis, Carnegie Institute of Technology, 1955 (unpublished).

[25]B. L. Moiseiwitsch and S. G. Stockman, J. Phys. B **13**, 2975 (1980).

[26]S. I. Salem and C. W. Schultz, At. Data **3**, 215 (1971).

[27]T. J. Gray, G. M. Light, R. K. Gardner, and F. D. McDaniel, Phys. Rev. A **12**, 2393 (1975).

[28]K. Ishii, S. Morita, H. Tawara, H. Kaji, and T. Shiokawa, Phys. Rev. A **11**, 119 (1975).

[29]T. K. Li, D. L. Clark, and G. W. Greenlees, Phys. Rev. Lett. **37**, 1209 (1975).

[30]R. Anholt (unpublished).